JPhys Photonics

RECEIVED
6 June 2019

REVISED
3 December 2019

ACCEPTED FOR PUBLICATION
2 January 2020

PUBLISHED
21 January 2020

PAPER

Magnetic field sensors in fused silica fabricated by femtosecond laser micromachining

João M Maia[1,2], **Vítor A Amorim**[1,2], **Duarte Viveiros**[1,2] and **P V S Marques**[1,2]

[1] CAP—Centre for Applied Photonics, INESC TEC, Porto 4169-007, Portugal
[2] Faculty of Sciences of University of Porto, Porto 4169-007, Portugal

E-mail: joao.m.maia@inesctec.pt

Keywords: Fabry–Pérot interferometer, femtosecond laser micromachining, ferrofluid, magnetic field sensing, wet etching

Abstract

Based on the characteristics of ferrofluids, a monolithic optofluidic device for magnetic field sensing is proposed and demonstrated. The device consists of a Fabry–Pérot interferometer, composed by an optical waveguide orthogonal to a microfluidic channel, which was fabricated inside a fused silica substrate through femtosecond laser micromachining. The interferometer was first optimized by studying the influence of the waveguide writing parameters on its spectral properties. Waveguides written at higher pulse energies led to a decrease of the signal-to-noise ratio, due to an enhancement of micrometer sized defects associated with Mie scattering. Fringe visibility was also maximized for waveguides written at lower scanning speeds. Making use of the tunable refractive index property exhibited by magnetic fluids, the interferometer was then tested as a magnetic field sensor by injecting a ferrofluid inside the microfluidic channel. A linear sensitivity of −0.25 nm/mT was obtained in the 9.0–30.5 mT range with the external field parallel to the waveguide axis.

1. Introduction

Magnetic fluids are stable colloidal suspensions of single-domain nanoparticles that are randomly dispersed in an aqueous or nonpolar solvent. Under an external magnetic field, and above a critical magnitude, the nanoparticles agglomerate along the field lines and form a chain-like structure, thereby making the ferrofluid spatially anisotropic [1]. As the field strength keeps increasing, these columns grow in both length and number, until a saturation state is reached. When the external field is removed, Brownian motion takes over and the nanoparticles redisperse in the carrier medium.

The alteration in the microstructure, induced by the external field, changes the optical properties of the ferrofluid. Namely, refractive index [2], field-dependent transmission [3], birefringence and dichroism [4] are all affected by the application of a magnetic field. Taking advantage of the field-induced modifications, several photonic devices for magnetic field sensing or for light modulation have been developed. Using the tunable refractive index property, multimode fibers have been used as modal interferometers, where lower-order modes interfere with higher-order modes whose propagation constant is affected by the ferrofluid that covers the fiber [5]. To increase the evanescent interaction with the surrounding ferrofluid and, consequently, the sensitivity, other methods, such as bending of multimode fibers [6], tapering [7] or the use of D-shaped fibers [8] have been adopted. Extrinsic fiber-based Fabry–Pérot interferometers have also been constructed by axially aligning two optical fibers and leaving a gap between them, which is filled with a magnetic fluid [9]. Sagnac interferometers have also been used to detect either the magnetic field strength or orientation due to the birefringence and dichroism properties [10, 11]. In [12], the spectral properties of a uniform and of a chirped Bragg grating were actively changed by controlling the position of a magnetic fluid that surrounds the grating. Light modulation, up to 50 Hz, was also shown in [13], by actuating on a ferrofluid plug that intersects the light path.

Compared to existent fiber-based sensors, planar devices offer the chance of simultaneous detection of magnetic field strength and its direction across all three dimensions. In addition, the advances made in femtosecond (fs) laser micromachining enable the design of complex geometries and the construction of

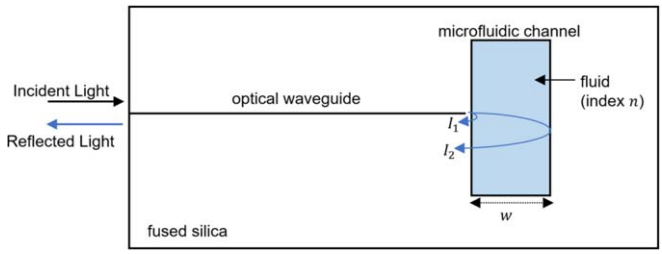

Figure 1. Layout of the proposed Fabry–Pérot interferometer. The refractive index of the fluid (n) changes with the magnitude of the external field (H).

monolithic optofluidic sensors, where optical elements interact directly with a fluidic medium circulating inside a microfluidic channel [14]. The fs-laser-induced modification can be used to increase the refractive index around the focal volume, resulting in the formation of optical circuits [15], and/or to enhance the etch rate of laser-affected zones relative to the bulk material, leading to a highly-selective and anisotropic etching reaction that enables the fabrication of three-dimensional microfluidic devices [16]. Using this technique we fabricated a Fabry–Pérot interferometer inside a fused silica substrate [17], and briefly explored its potential as a magnetic field sensor, by injecting a ferrofluid inside the cavity. Here, we fabricate a similar device and further study its response. First, we tested the interferometer as a refractive index sensor and, through these results and based on the conclusions of [15], we optimized the waveguide writing parameters to yield a signal with both high signal-to-noise ratio (SNR) and visibility. Then, we showcase the device's ability to sense magnetic field, and study the role of the channel's surface chemistry in stabilizing the ferrofluid.

2. Experimental procedure

2.1. Device layout and operation

The layout of the device is shown in figure 1: an optical waveguide is written orthogonally to a microfluidic channel/cavity that is filled with a fluid. The device behaves as a low-finesse Fabry–Pérot interferometer, because the reflection is determined solely by the Fresnel coefficients. Therefore, the interference can be described as an interaction between two waves. The interferometer can be analyzed by measuring the reflected intensity (I_r), which is given by [18]:

$$I_r = I_1 + I_2 + 2\sqrt{I_1 I_2}\cos\delta, \tag{1}$$

where I_1 and I_2 are the intensities of the light beams that travel through paths 1 and 2 (figure 1), respectively. The phase difference δ between both waves is defined as:

$$\delta = \frac{2\pi}{\lambda}\cdot(\Delta L)\cdot n, \tag{2}$$

where λ is the light wavelength, ΔL is the path difference between both beams (i.e. twice the cavity width w), and n is the cavity refractive index. The condition for constructive interference is reached when the phase difference is equal to $2m\pi$, where m is an integer. Or, in other words, the measured spectrum shows a peak when the wavelength is given by:

$$\lambda_m = \frac{n\cdot\Delta L}{m}. \tag{3}$$

From equation (3), it can be concluded that whenever the refractive index of the medium inside the cavity changes, the resulting spectrum will shift towards the lower (higher) wavelength side, depending if the index decreases (increases).

2.2. Fabrication

A fiber amplified fs-laser system (Amplitude Systèmes HP), emitting a second harmonic beam at 515 nm with an approximate pulse duration of 250 fs at 500 kHz, was used to fabricate the device. The linearly polarized beam was focused inside a fused silica substrate (Suprasil 1) with a 0.55 numerical aperture aspherical lens (New-Focus 5722-A-H) emplaced in a vertical piezostage (PI P-725.4CD PIFOC). The substrate was mounted on X–Y air-bearing linear stages (Aerotech ABL10100-LN) and translated in relation to the beam focus. The waveguide and the microfluidic channel were written sequentially to ensure perfect alignment between both.

The optical waveguides were written 55 μm below the silica surface, with the polarization of the laser beam set parallel to the writing direction. Several 1.3 cm long waveguides were written with energies of 50, 75, 100 and

200 nJ at scanning speeds of 50, 100, 200 and 400 μm s^{-1}. All waveguides were written on the same direction to avoid the Quill effect [19].

The microfluidic channel was written from the bottom to the top by stacking multiple adjacent modification tracks with a 2 and 3 μm spacing (horizontal and vertical, respectively), at a scanning speed of 500 μm s^{-1}, pulse energy of 80 nJ and with the polarization of the beam set orthogonal to the scanning direction. These conditions ensure low sidewall surface roughness [20], leading to specular reflection of light in the channel walls. Like in the case of optical waveguides, the modification tracks were all written in the same direction.

Wet etching was done in an ultrasonic cleaner (Branson 2510) by immersing the substrate in a 10% hydrofluoric (HF) acid solution for 105 min. The resulting channel width is not uniform in depth, being larger at the top, with a deviation from the vertical of 5° utmost. This effect, resultant from the finite HF etching selectivity, leads to a reduction of the light coupled to the waveguide, from light travelling through the cavity, due to reflection/refraction at non-normal incidence. The channel has a final depth of 90 μm and a width (w) of 37 μm, with the waveguides terminating 10 μm from the channel wall. The substrate's edge facets were polished after etching in order to eliminate the waveguide's etched input/output section, thereby improving light coupling.

To characterize the Fabry–Pérot, light from a broadband source (EXFO Optical System IQ-203 with an integrated ASE source module IQ-2300), ranging from 1450 to 1650 nm, is injected into an optical circulator and coupled into a single-mode fiber (SMF-28 with APC termination to avoid back-reflections) that is butt-coupled to the waveguide. The reflected light is guided back into the circulator and detected by an optical spectrum analyzer (Yokogawa AQ3670D), with a resolution of 1 nm. The substrate was mounted on a 5-axis stage (Elliot Martock MDE881 stage with piezocontrols Dali E-2100) for precise alignment of the optical fiber with the waveguide. Index matching (Cargille series AA $n_D^{25\,^\circ\mathrm{C}} = 1.4580 \pm 0.0002$) was used to minimize Fresnel reflections at the input/output facet.

For magnetic field characterization, the device was placed inside a magnetic field generation coil. The field strength can be controlled by changing the electrical current flowing through the coil, while its orientation can be manipulated by rotating the coil in relation to the waveguide axis.

3. Experimental results and discussion

3.1. Refractive index characterization

Different solutions were used to characterize the Fabry–Pérot's response to refractive index. First, the reflected spectra of the empty channels were measured, corresponding to an index $n = 1.0003$ at 1550 nm. Then, different Cargille series AAA solutions were tested, with refractive indexes at 1550 nm of $n = 1.2962$, $n = 1.3058$, $n = 1.3154$, $n = 1.3538$, $n = 1.3731$, and $n = 1.3826 \pm 0.0002$. These liquids show negligible dispersion and absorption throughout the entire measurement range. The fluids were drawn into the channels by capillarity and, through microscope observations, we confirmed no air-bubbles had been formed in the channel. In between measurements, the substrate was cleaned with ethanol and deionised water in an ultrasonic bath.

After characterizing the Fabry–Pérot interferometers, it is visible that the waveguide writing parameters influence the quality of the reflected signal. For instance, the signal of figure 2(a) is less noisy than the signal of figure 2(c), as less fluctuations of the reflected power are observed. To understand the origin of this noise, we first determined the Fourier transform of each signal, for all refractive indexes. In figures 2(b) and (d), we see that the Fourier spectrum shows a dominant peak, located at the cavity width, corresponding to the interference between the light beams reflected at the first and second channel sidewall-silica interface. In consequence, the observed noise is random and is not related to interferences originated at the fiber-waveguide interface or in the circulator.

To quantify the noise, we then calculated the SNR of each spectrum, by determining the ratio between the signal and noise root-mean-squares. The noise component was taken by subtracting the measured signal from a smoothed curve, obtained by applying a Savitsky–Golay filter to the measured signal. In figure 3(a), we observe that, for a certain refractive index, the SNR decreases when the pulse energy increases. To a lower extent, this trend is also observed when the scanning speed increases, as can be seen in figure 3(b). A similar effect was also observed for channels of different width, which further supports that this behavior is related to the waveguide writing process. We believe this effect is due to inhomogeneities formed within the optical waveguide during the fabrication, leading to random reflections that manifest as arbitrary interferometers, causing unexpected fluctuations in the output spectrum. These fluctuations also appear as smaller peaks in the Fourier spectrum of noisier signals, as displayed in figure 2(d). In a previous work [15], using the same laser direct writing unit, glass medium and writing parameters, the loss mechanisms of fs-laser written optical waveguides were studied. It was shown that the waveguide's propagation losses were affected by both Rayleigh and Mie scattering, whose coefficients could be controlled by the writing parameters. The Rayleigh scattering coefficient was shown to

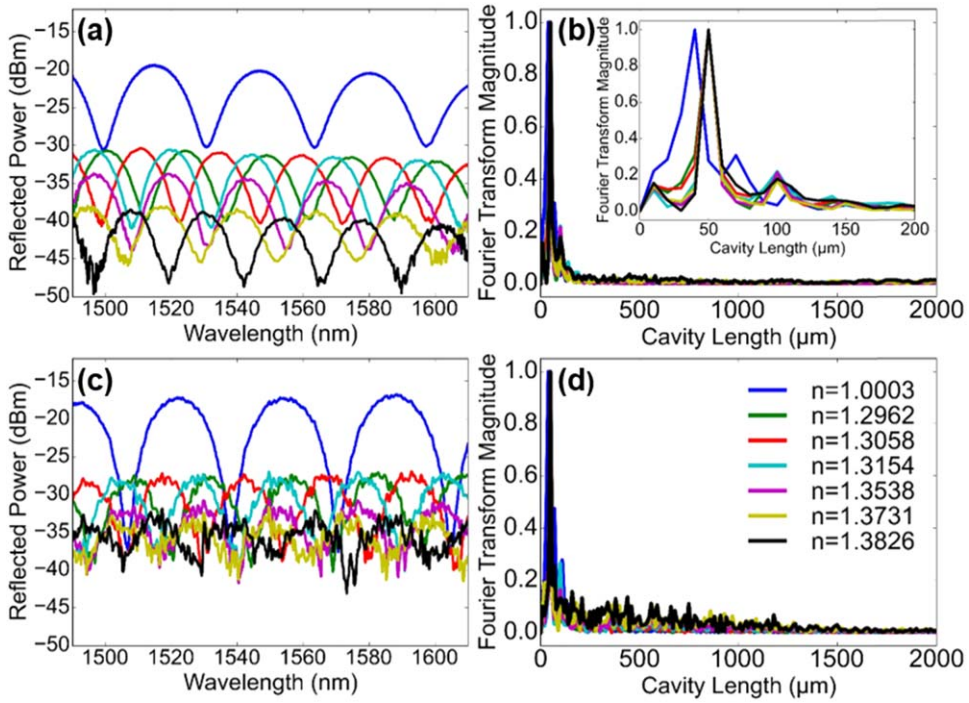

Figure 2. Reflected spectra of a Fabry–Pérot interferometer with a 37 μm wide cavity and with an optical waveguide written at (a) 75 nJ and 50 μm s^{-1}, and at (c) 200 nJ and 400 μm s^{-1}, for several refractive indexes inside the cavity. Figures (b) and (d) show the respective Fourier transform. The inset of image (b) shows a zoom-in of the Fourier transform, where it can be seen that the peak is located at the width of the microfluidic channel.

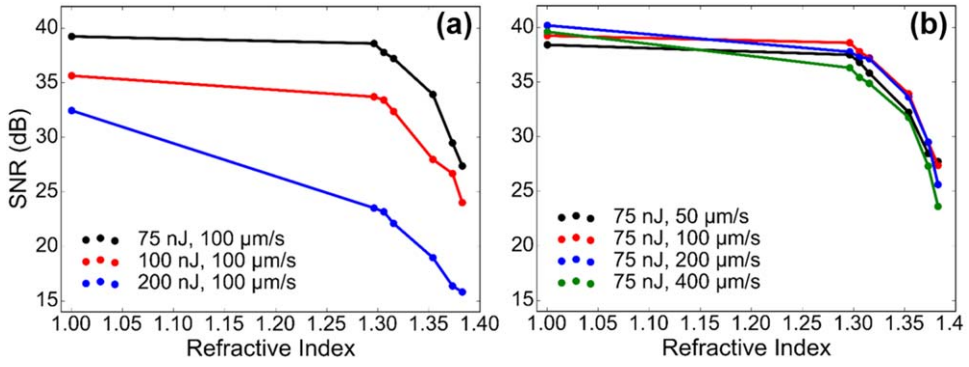

Figure 3. SNR, as a function of the cavity refractive index, for a 37 μm wide cavity and waveguides written at different (a) energies and (b) scanning speeds.

increase with the scanning speed and, in our configuration, was maximum for a pulse energy of 200 nJ. Its influence is wavelength-dependent, being negligible in the range of wavelengths tested in this work. On the other hand, the Mie scattering coefficient increased with pulse energy, being almost independent of the scanning speed, which is similar to the trend observed here. Therefore, this evidence suggests that the SNR has its origin on the same defects that cause Mie scattering within the optical waveguide [15]. Furthermore, the noise level is seen to decrease as the interferometer length increases up to 1.5 mm (figure 2(d)). These dimensions are of the order of those required by the defects for Mie scattering at these wavelengths, further supporting the fact that the interference is occurring between this type of defects. Also, the decrease in noise level demonstrates that the interference between defects placed farther away is less likely, as the intensity of the reflected wave quickly decreases with the number of reflections. Figure 3 also shows that the SNR decreases with the cavity refractive index. This result is a direct consequence of the lower Fresnel reflection coefficient, observed when the fused silica and the cavity refractive index become closer, and has more to do with a decrease in the signal intensity than with an increase of the noise intensity, as can be confirmed from figures 2(a) and (c).

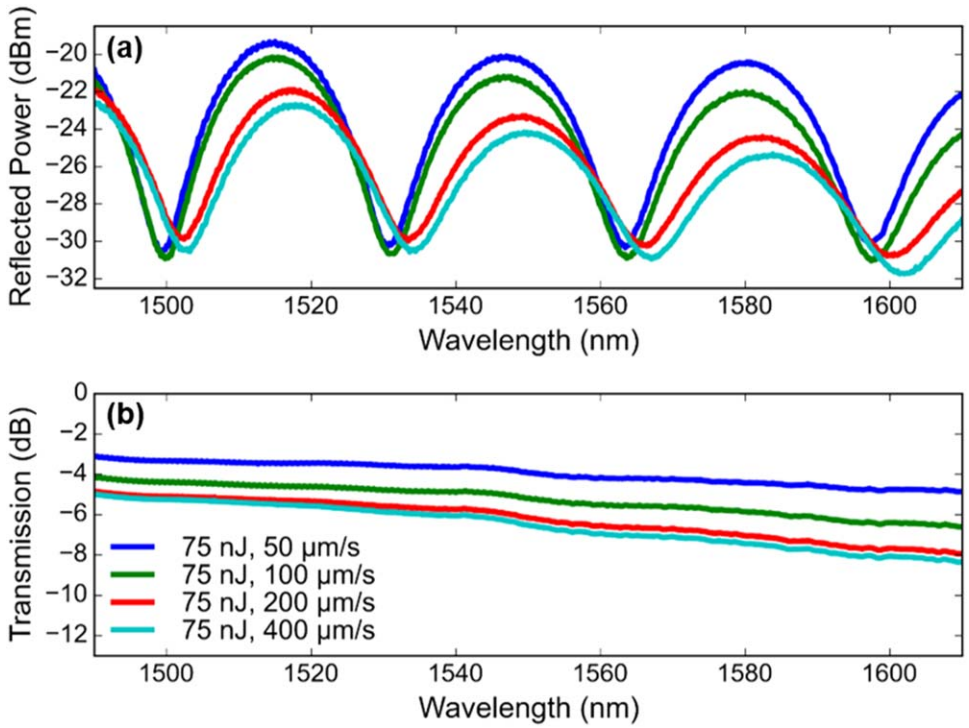

Figure 4. (a) Reflected spectra of a Fabry–Pérot interferometer with a 37 μm wide cavity, with waveguides written with an energy of 75 nJ at varying scanning speeds, and (b) transmitted intensity of 2.5 cm long waveguides fabricated at said parameters. In all measurements, the cavity is empty.

Although waveguides written at 75 nJ show maximum SNR, figure 4(a) also reveals that the fringe visibility is influenced by the scanning speed. In particular, fringe visibility decreases when the scanning speed increases, again regardless of the channel width and of the cavity refractive index. The optimization of this parameter is also relevant, as it is related to the ease with which we can distinguish the resonant peaks and, therefore, it affects the measurement resolution. The fringe visibility depends on the relative intensity of both interfering beams: if equal, then the visibility is maximum otherwise, if the intensity of one beam is much higher than of the other, it is minimum and no modulation is observed in the measured spectrum. Here, we can affirm that the intensity (I_1) of the beam reflected at the first interface (path 1 in figure 1) is practically independent of the fabrication parameters due to the small free-space propagation distance, depending mostly on the Fresnel reflection coefficient. Consequently, the visibility is mainly determined by the intensity (I_2) of the beam that propagates through the cavity (path 2 in figure 1). The intensity of the latter is mainly determined by the waveguide's acceptance/emission angle and by the orthogonality of the channel sidewall, which dictate the amount of light coupled back into the waveguide. Normally, a smaller acceptance angle would be preferred, since beam divergence leads to an enlargement of the beam radius after travelling through the cavity, thereby diminishing the amount of captured light [21]. However, since the refraction at the channel sidewall occurs at non-normal incidence, as a result of the channel's angular deviation, a smaller beam divergence renders a worse coupling of light back to the waveguide. In consequence, the intensity of the beam (I_2) and, in turn, the visibility, are enhanced for waveguides with higher acceptance angle. In figure 4(b), we observe that the transmitted power of straight waveguides decreases when the scanning speed increases, which is due to the smaller laser-induced index modification, as is explained in [15]. Therefore, the numerical aperture and acceptance angle of the waveguide decrease when the scanning speed increases, explaining the lower visibilities observed in figure 4(a). Although higher fringe visibilities can be obtained with waveguides written with higher pulse energy, due to the higher numerical aperture, this is done at the expense of a lower SNR. It should also be noted that the coupling losses at the optical fiber-waveguide interface also increase with the wavelength and the scanning speed used, due to the increasing mode mismatch between the fiber and the waveguide mode [15]. This translates into a signal with less power travelling to and from the cavity, hence the similarities between the waveguide transmission and the cavity reflection spectra shown in figure 4. Still, further studies are necessary to understand how the waveguide writing parameters and its termination shape, the distance between the waveguide and the channel, and the channel shape influence the visibility. Nevertheless, for all cavities we see that the visibility is maximized for waveguides written at low scanning speeds. In addition, fringe visibility decreases when the cavity width

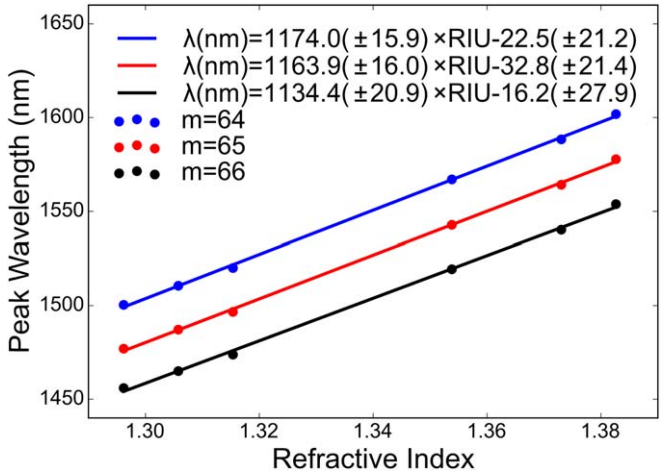

Figure 5. Peak wavelength as a function of the refractive index for a Fabry–Pérot interferometer with cavity width of 37 μm, for three interference orders.

increases [21]. In separate experiments, we observed that for widths ranging from 17 to 47 μm, this parameter remains essentially unchanged.

Finally, the sensitivity to refractive index of Fabry–Pérot interferometers written with a pulse energy of 75 nJ and scanning speed of 50 μm s^{-1} was calculated, as depicted in figure 5. For a 37 μm wide cavity, the signal red-shifts with the increase of the cavity refractive index, with a maximum linear sensitivity of 1174.0 $\pm$ 15.9 nm/RIU (refractive index unit) being measured in the range of 1.2962–1.3828 (both at 1550 nm) for the interference order m equal to 64. Figure 5 also shows that the sensitivity ($d\lambda/dn$) is inversely proportional to the order m, as is expected from equation (3).

3.2. Magnetic field detection

If the microfluidic channel is filled with an active material whose refractive index changes under an external field, the interferometer can then be used as a magnetic field sensor. For this application, an optical waveguide was written at 75 nJ and 50 μm s^{-1}, with the beam polarization set parallel to the scanning direction, in order to maximize SNR and visibility. When choosing the microfluidic channel, it is important to note that, with ferrofluids, the visibility tends to decrease further due to the ferrofluid's high optical loss. In the end, we opted for a 37 μm wide microfluidic channel. The ferrofluid optical absorption also increases with the concentration of magnetic nanoparticles [22], further diminishing the visibility. Therefore, a water-based ferrofluid (EMG507, Ferrotec Inc.), composed by magnetite (Fe_3O_4) nanoparticles with an average diameter of 10 nm dispersed in a volume concentration of 0.4%–1.1% was used. A PDMS (polydimethylsiloxane) layer, with an inlet and an outlet, was permanently bonded to the silica substrate, after O_2-plasma treatment of the surfaces of the silica substrate and PDMS layer. A syringe, connected to a microfluidic tubing with outer diameter of 1/16' that was fitted into the inlet, pumped the ferrofluid into the channel. After injection, the tubing was removed, and another glass sample was permanently bonded to the PDMS layer to avoid rapid evaporation of the ferrofluid through the inlet/outlet. No air-bubbles were observed inside the microfluidic channel.

Right after the ferrofluid was injected, we measured the reflected spectrum, which exhibited the expected profile, as can be seen in figure 6. Without any external field, the spectrum remained constant, indicating that the nanoparticles were randomly dispersed in the carrier liquid. When an external field is applied parallel to the waveguide axis, the reflected spectrum shifts to the shorter wavelength side. According to equation (3) and to figure 5, and because thermally-induced variations of the cavity width can be neglected, the blue-shift means that the cavity's refractive index decreases. After removing the field, the nanoparticles should re-disperse in the fluid due to Brownian motion, and we should retrieve the initial spectrum, given that the nanoparticles show no remnant magnetization. However, from figure 6 we observe that the reflected spectrum does not resemble the initial one and that the visibility is practically null. Microscope observations reveal that the ferrofluid is still inside the microfluidic channel. At the same time, if the nanoparticles were to deposit in the bottom of the channel, the measured spectrum would correspond to that of the carrier liquid, i.e. water, and, consequently, the fringe visibility would be higher given that water shows negligible absorption in the measured wavelength range. Therefore, other effects must be in play. If we apply, once again, a magnetic field, with the same magnitude and orientation as before, the visibility increases, and we can recover the initial spectrum to some extent.

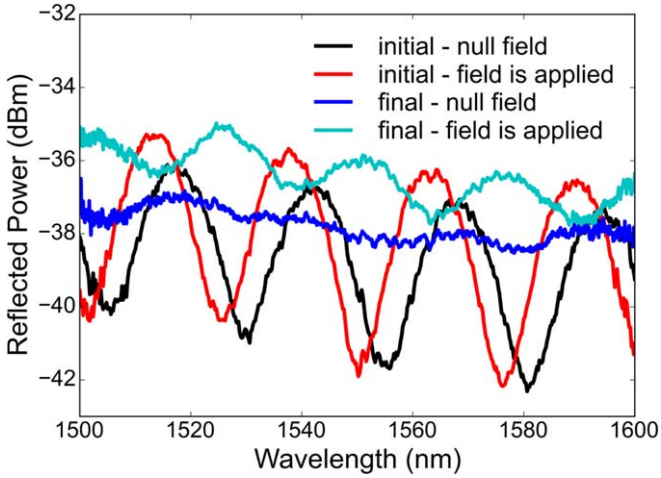

Figure 6. Reflected spectra, at different instances, for a Fabry–Pérot cavity with magnetic fluid (EMG507, Ferrotec Inc.).

Nevertheless, the location of the maxima wavelength shifts, indicating that the cavity refractive index has changed.

We believe this behavior is related to an alteration in the distribution of magnetic nanoparticles inside the cavity. Konstantaki *et al* noticed that magnetic fluids tend to leave a residue layer that adheres to the surface of an optical fiber [23]. In that work, the issue was solved by silanizing the fiber surface and mixing the ferrofluid with an immiscible solution. Here, because the fused silica substrate was etched with HF acid, the inner walls of the channel also present H^+ groups, which amplifies the problem by causing a weak acid-base reaction between the alkaline nanoparticles (pH $=$ 8–9) and the acidic channel surface [24]. The adhesion of the nanoparticles to the channel sidewalls causes scattering and attenuation of the propagating light beam, leading to the degradation of the optical signal. This residue layer can be partially broken if the external field is again applied, which leads to the slight recovery of the spectrum, as shown in figure 6.

To avoid adhesion, the surface of the channel must be treated with an alkaline or oxidizing agent that will increase the pH of the channel walls. Two solutions were tested: hydrogen peroxide (H_2O_2) and potassium hydroxide (KOH). The treatment with H_2O_2, although it increased the device lifetime, did not fully correct this problem. KOH, because it is more reactive and is also a fused silica etchant, is better suited for this function. Treatment with KOH was done by placing the substrate in ultrasonic agitation (Cole-Parmer 8891) in a solution of KOH with a concentration of 40.02% (mass per volume) at 48 °C for six hours. At this temperature, we estimate that 100 nm of the silica layer were removed [25].

After surface treatment, we observed that the waveguide entrance on the substrate's facet is slightly etched, which leads to an increase in the coupling losses from the fiber to the waveguide and, consequently, to a decrease in the intensity of the reflected signal, as seen in figure 7. The visibility also tends to decrease with time, although much slower than in the original case and after H_2O_2 treatment, as the adhesion issue is still not completely solved. Nevertheless, treatment with KOH improves the device lifetime up to four days, enabling its application as a magnetic field sensor.

Figures 7 and 8 show the sensor response to the magnetic field magnitude, with the field applied parallel to the waveguide axis. The measurements were carried at 19.0 °C $\pm$ 0.5 °C, so index variations induced by thermal effects can be neglected; thermal cross talk can be completely avoided by adding a Bragg grating [26]. For field strengths below 9 mT, no significant variations are observed in the spectrum, as the exerted magnetic force is not enough to overcome diffusive forces and, in turn, form magnetic columns that cause the index variation [1]. From 9 mT onwards, we observe a blue-shift with the increase of field strength, indicating that the ferrofluid's index is decreasing, as explained previously. The peak wavelength was determined from a Python script: the spectra was first smoothed through a Savitsky–Golay filter, the derivative of the resulting curves was then calculated, and the wavelength was determined by checking where the derivative changes signal. A linear sensitivity of -0.25 ± 0.02 nm/mT was measured in the 9.0–30.5 mT range. Higher fields were not tested due to hardware limitations. Compared to [17], the sensitivity increases from -0.12 to -0.25 nm/mT. This is probably due to the fact that, in [17], the channel was not treated in KOH, which causes the nanoparticles to adhere to its surface, thereby reducing the concentration of nanoparticles dispersed in the carrier liquid. In turn, for the same field magnitude, less magnetic columns are formed, leading to a smaller index variation and sensitivity in [17].

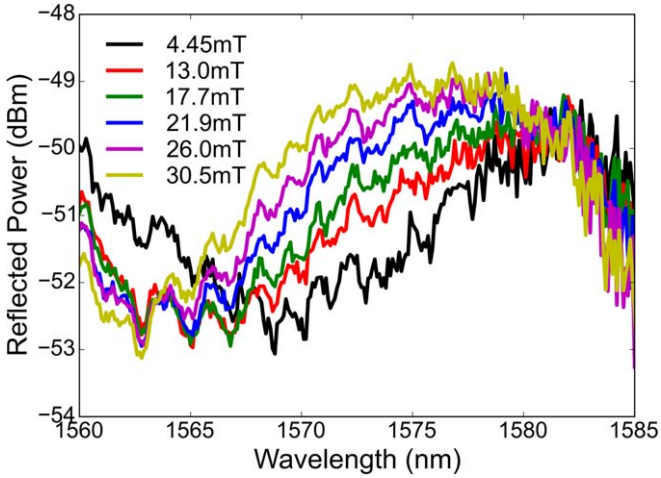

Figure 7. Reflected spectra at different magnetic field magnitudes.

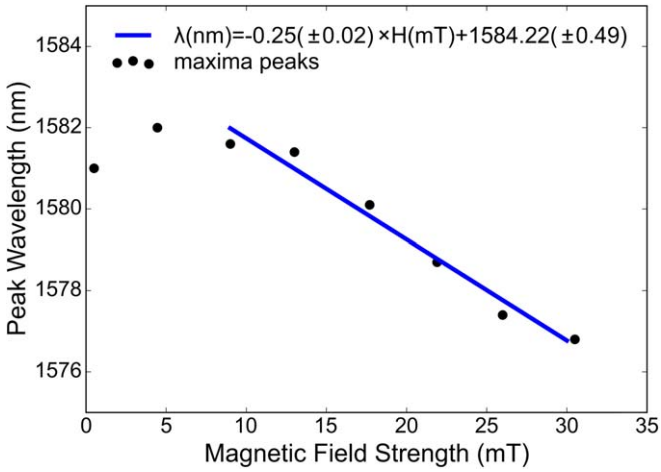

Figure 8. Peak wavelength as a function of the magnetic field magnitude.

In similar fiber-based Fabry–Pérot interferometers, sensitivities of 1.21 nm/mT in the 6 to 18 mT range with a 3.9% volume concentration of magnetic nanoparticles [27], and 2.3 nm/mT in the 0–12 mT range with a 17.7% concentration [9] were obtained. As can be seen, higher sensitivities can be obtained with ferrofluids with higher concentration of magnetic nanoparticles, but at the expense of smaller fringe visibilities, leading, in consequence to a lower resolution. Zu *et al* also observed that adhesion to the channel walls is more probable to happen with ferrofluids with higher concentration of magnetic nanoparticles [28]. In the previously mentioned papers, the spectrum red-shifts with the increase in field strength, indicating that the ferrofluid refractive index is increasing, contrarily to the behavior we observe. This difference is due to the orientation between the magnetic field and the light propagation direction [1]. As the external field is applied, the nanoparticles form magnetic chains aligned parallel to the waveguide axis [1]. In turn, the refractive index seen by the waveguide decreases from the ferrofluid's refractive index (1.3414 at 1550 nm and with null field [1]) to the index of the carrying fluid, i.e. water (1.318). For this reason, the sensitivity shows a negative signal.

After one week, the fluid is fully evaporated, creating a cluster of magnetic nanoparticles at the bottom of the channel. From the diffusion coefficient of water (the ferrofluid's carrier liquid) in PDMS and fused silica, which is 10^{-9} m^2 s^{-1} and 10^{-17} m^2 s^{-1} respectively [29, 30], it is evident that the evaporation issue resides in the PDMS. Thus, more definite sealing methods must be used. A possible alternative is to produce a full silica-based device by laser-welding a glass cover, which shows a lower diffusion coefficient, to the silica substrate containing the microfluidic channel [31].

Therefore, we believe that using a monolithic optofluidic device, where more optical functions can be implemented on the same substrate with fluid handling capabilities being ensured by the microfluidic layer, offers the best approach to this type of sensors based on magnetic fluids.

4. Conclusion

This work discusses the fabrication of Fabry–Pérot interferometers, through fs-laser micromachining, in fused silica. The SNR of the reflected spectrum was analysed in relation to the waveguide's writing parameters. At high pulse energies, the SNR decreases due to the creation of defects associated with Mie scattering, which introduces random reflections throughout the waveguide as well as phase variations that result on a random modulation of the reflected signal. The fringe visibility was also found to be lower for waveguides written at higher scanning speeds, which we suspect to be related to the decreasing waveguide's numerical aperture that results in a lower acceptance angle and, in turn, to a smaller percentage of light recoupled back into the waveguide and lower visibility. Optimal SNR and visibility were found for waveguides written at a pulse energy of 75 nJ and a scanning speed of 50 μm s^{-1}, with a beam polarization parallel to the writing direction, regardless of the channel width. For a 37 μm wide cavity, a maximum linear sensitivity of 1174.0 $\pm$ 15.9 nm/RIU was determined for refractive indexes ranging from 1.2962 to 1.3824 (at 1550 nm).

Due to the tunable refractive index property of ferrofluids, the same Fabry–Pérot interferometer was used to measure magnetic field strength. The microfluidic channel surface was treated with KOH at 48 °C to avoid adhesion of the magnetic nanoparticles to the channel walls, due to a weak acid-base interaction. A linear sensitivity of −0.25 nm/mT, from 9.0 to 30.5 mT, with the field parallel to the waveguide axis was measured. Although treatment with KOH increased the device lifetime, more definitive solutions should be implemented. Future developments, such as simultaneous detection of field strength and orientation can be envisioned by writing waveguides spanning all spatial directions.

Acknowledgments

This work was supported by Fundação para a Ciência e Tecnologia through grant no. SFRH/BD/133095/2017. The results presented in this paper are part of the Project 'On Chip Whispering Gallery Mode Optical Microcavities for Emerging Microcontaminant Determination in Waters'—SAFE WATER, supported and co-founded by the European Commission, Directorate-General Communications Networks, Content and Technology (DG-CONNECT) under the ERA-NET Confund scheme—Horizon 2020 'Horizon 2020—the Framework Programme for Research and Innovation (2014–2020)'.

ORCID iDs

João M Maia https://orcid.org/0000-0001-9260-4247

References

[1] Zhao Y, Wu D, Lv R-Q and Ying Y 2014 *IEEE Trans. Magn.* **50** 6763086
[2] Hong C-Y, Yang S Y, Horng H E and Yang H C 2003 *J. Appl. Phys.* **94** 3849–52
[3] Yang S Y, Chiu Y P, Jeang B Y, Horng H E, Hong C-Y and Yang H C 2001 *Appl. Phys. Lett.* **79** 2372–4
[4] Di Z, Chen X, Pu S, Hu X and Xia Y 2006 *Appl. Phys. Lett.* **89** 211106
[5] Chen Y, Han Q, Liu T, Lan X and Xiao H 2013 *Opt. Lett.* **38** 3999–4001
[6] Zhang R, Liu T, Han Q, Chen Y and Li L 2014 *Appl. Phys. Express* **7** 072501
[7] Miao Y, Wu J, Lin W, Song B, Zhang H, Zhang K, Liu B and Yao J 2014 *J. Lightwave Technol.* **32** 6922594
[8] Violakis G, Korakas N and Pissadakis S 2018 *Opt. Lett.* **43** 142–5
[9] Homa D and Pickrell G 2014 *Sensors* **14** 3891–6
[10] Zu P, Chan C C, Lew W S, Jin Y, Zhang Y, Liew H F, Chen L H, Wong W C and Dong X 2012 *Opt. Lett.* **37** 1425–7
[11] Wei F, Mallik A K, Liu D, Wu Q, Peng G-D, Farrell G and Semenova Y 2017 *Sci. Rep.* **7** 4725
[12] Candiani A, Margulis W, Sterner C, Konstantaki M and Pissadakis S 2011 *Opt. Lett.* **36** 2548–50
[13] Gu Y, Valentino G and Mongeau E 2014 *Appl. Opt.* **53** 537–43
[14] Osellame R, Cerullo G and Ramponi R 2012 *Femtosecond Laser Micromachining: Photonic and Microfluidic Devices in Transparent Materials* vol 14 1st edn (Berlin: Springer) pp 389–420
[15] Amorim V A, Maia J M, Viveiros D and Marques P V S 2019 *J. Lightwave Technol.* **37** 2240–5
[16] Hnatovsky C, Taylor R S, Simova E, Rajeev P P, Rayner D M, Bhardwaj V R and Corkum P B 2006 *Appl. Phys.* A **84** 47–61
[17] Maia J M, Amorim V A, Viveiros D and Marques P V S 2019 *EPJ Web Conf.* **215** 13001
[18] Lin C-H, Jiang L, Xiao H, Chai Y-H, Chen S-J and Tsai H-L 2009 *Opt. Lett.* **34** 2408–10
[19] Kazansky P G, Yang W, Bricchi E, Bovatsek J, Arai A, Shimotsuma Y, Miura K and Hirao K 2007 *Appl. Phys. Lett.* **90** 151120
[20] Maia J M, Amorim V A, Alexandre D and Marques P V S 2017 *J. Lightwave Technol.* **35** 2291–8
[21] Zhang Y, Li Y, Wei T, Lan X, Huang Y, Chen G and Xiao H 2010 *IEEE Photonics J.* **2** 469–81
[22] Horng H E, Yang S Y, Tse W S, Yang H C, Luo W and Hong C-Y 2002 *J. Magn. Magn. Mater.* **252** 104–6
[23] Konstantaki M, Candiani A and Pissadakis S 2011 *J. Eur. Opt. Soc., Rapid Publ.* **6**
[24] Park Y C, Paulsen J, Nap R J, Whitaker R D, Mathiyazhagan V, Song Y-Q, Hürlimann M, Szleifer I and Wong J Y 2014 *Langmuir* **30** 784–92
[25] Pfiffer M, Cormont P, Fargin E, Bousquet B, Dussauze M, Lambert S and Néauport J 2017 *Opt. Express* **25** 4607–20

[26] Xia J, Wang F, Luo H, Wang Q and Xiong S 2016 *Sensors* **16** 620
[27] Song Y, Yuan L, Hua L, Zhang Q, Lei J, Huang J and Xiao H 2016 *Proc. SPIE* **9750** 97501U
[28] Zu P, Chan C C, Gong T, Jin Y, Wong W C and Dong X 2012 *Appl. Phys. Lett.* **101** 241118
[29] Watson J M and Baron M G 1996 *J. Membr. Sci.* **110** 47–57
[30] Wakabayashi H and Tomozawa M 1989 *J. Am. Ceram. Soc.* **72** 1850–5
[31] Richter S, Döring S, Tünnermann A and Nolte S 2011 *Appl. Phys.* A **103** 257–61